Galaxy Infall Kinematics as a Test of Modified Gravity

Ying Zu[1][*], David H. Weinberg[1], Elise Jennings[2], Baojiu Li[3], Mark Wyman[2,4],

1 *Department of Astronomy and CCAPP, The Ohio State University, 140 W. 18th Avenue, Columbus, OH 43210, USA*
2 *The Kavli Institue for Cosmological Physics and Enrico Fermi Institute, University of Chicago, 5640 South Ellis Avenue, Chicago, IL 60637, USA*
3 *Institute for Computational Cosmology, Department of Physics, Durham University, Durham DH1 3LE, UK*
4 *Center for Cosmology and Particle Physics, Department of Physics, New York University, New York, NY, 10003, U.S.A.*

ABSTRACT
Infrared modifications of General Relativity (GR) can be revealed by comparing the mass of galaxy clusters estimated from weak lensing to that from infall kinematics. We measure the 2D galaxy velocity distribution in the cluster infall region by applying the galaxy infall kinematics (GIK) model developed by Zu & Weinberg (2013) to two suites of $f(R)$ and Galileon modified gravity simulations. Despite having distinct screening mechanisms, namely, the Chameleon and the Vainshtein effects, the $f(R)$ and Galileon clusters exhibit very similar deviations in their GIK profiles from GR, with $\sim$ 100–200 km/s enhancement in the characteristic infall velocity at $r = 5\,h^{-1}\mathrm{Mpc}$ and 50–100 km/s broadening in the radial and tangential velocity dispersions across the entire infall region, for clusters with mass $\sim 10^{14}\,h^{-1}M_\odot$ at $z = 0.25$. These deviations are detectable via the GIK reconstruction of the redshift–space cluster–galaxy cross–correlation function, $\xi^s_{cg}(r_p, r_\pi)$, which shows $\sim$ 1–2 $h^{-1}\mathrm{Mpc}$ increase in the characteristic line-of-sight distance $r_{\pi,c}$ at $r_p < 6\,h^{-1}\mathrm{Mpc}$ from GR predictions. With overlapping deep imaging and large redshift surveys in the future, we expect that the GIK modelling of ξ^s_{cg}, in combination with the stacked weak lensing measurements, will provide powerful diagnostics of modified gravity theories and the origin of cosmic acceleration.

Key words: galaxy: clusters: general — galaxies: kinematics and dynamics — cosmology: large-scale structure of Universe

1 INTRODUCTION

The late–time acceleration of the Universe can be explained by modifying General Relativity (GR) on cosmological scales, avoiding the need of invoking a cosmological constant Λ or an exotic repulsive fluid (a.k.a., dark energy). Many popular modified gravity (MG) theories rely on an extra scalar field ψ to mediate a fifth force,[1] making the distributions and motions of galaxies different from those predicted by GR (see Jain & Khoury 2010, and references therein). In particular, the coherent infall of galaxies onto massive clusters will exhibit systematic deviations due to the enhanced gravitational forces. Zu & Weinberg (2013, hereafter ZW13) demonstrated that in ΛCDM+GR simulations the velocity distribution of galaxies in the virial and infall regions of clusters (hereafter abbreviated GIK for galaxy infall kinematics) is well described by a 2–component velocity distribution model, which can be reconstructed from measurements of the redshift–space cluster–galaxy cross–correlation function, ξ^s_{cg}. In this paper, we apply GIK

modelling to two suites of different MG simulations and investigate the possible signals of MG imprinted on the redshift–space distribution of galaxies around clusters, using dark matter particles and halos as proxies for galaxies. (For more general discussions of clusters as tests of cosmic acceleration theories we refer readers to Weinberg et al. (2013), and for a succinct discussion of distinguishing MG from dark energy to Hu 2009.)

While deviations from GR may be welcomed on cosmological scales, a "screening" mechanism must be invoked in MG theories to recover GR in high density regions like the solar system, where GR has passed numerous stringent tests (e.g., Bertotti et al. 2003; Baeßler et al. 1999). Current viable screening mechanisms generally fall into two classes:

• The Chameleon–like mechanism, in which the self–interactions of the scalar field are regulated by a potential $V(\psi)$ (Buchdahl 1970; Khoury & Weltman 2004). Objects are screened when their gravitational potential $|\phi_{\mathrm{grav}}|$ is larger than $\bar\psi/\alpha$, where $\bar\psi$ is the cosmic mean of ψ and $\alpha \sim \mathcal{O}(1)$ is the coupling between matter and ψ. In other words, the effective scalar charge Q that responds to ψ is reduced by the ambient gravitational potential. This type of screening operates in $f(R)$ (Carroll et al. 2004; Capozziello et al. 2003; Nojiri & Odintsov 2003), sym-

metron (Hinterbichler & Khoury 2010; Olive & Pospelov 2008; Pietroni 2005)), and dilaton (Brax et al. 2011) theories. In this paper we will focus on the Chameleon mechanism within $f(R)$, where the Ricci scalar, R, in the Einstein–Hilbert action is replaced by $R + f(R)$ where $f(R)$ is an arbitrary function of R.[2]

• The Vainshtein mechanism, in which the self–interactions of the scalar field are determined by the derivatives of ψ, which suppress the scalar field and fifth force in high density regions (Vainshtein 1972; Babichev & Deffayet 2013). Scalar fields that exhibit Vainshtein screening are generally called 'Galileons' because of an internal Galilean symmetry (Nicolis et al. 2009). For an isolated spherical source, the force transition happens at a characteristic radius $r_* = (r_s r_c^2)^{1/3}$ (called the Vainshtein radius), where r_s is the Schwarzschild radius of the source and r_c in models of interest is on the order of the Hubble radius cH_0^{-1}. Within r_* the scalar field is suppressed ($\psi \propto \sqrt{r}$), forming a "sphere" of screened region around the source. This mechanism is at play in the Dvali–Gabadadze–Porrati (DGP, Dvali et al. 2000) and massive gravity (de Rham et al. 2011b) theories. For our purpose, we simplify this class of model as a theory with a ΛCDM background cosmology and an extra Galileon–type scalar field that manifests Vainshtein screening (Wyman et al. 2013).

In both the $f(R)$ and Galileon models, the maximum force enhancement is $4/3$ times the normal gravity, but the "fifth force" that produces this enhancement has different ranges in the two models. Since the Chameleon scalar field becomes Yukawa–screened, the fifth force does not have infinite range, i.e., it cannot reach to cosmological scales. Galileons, however, are never massive, so their force has an infinite range, thus having a much larger impact on linear perturbation theory than Chameleons do. In the local Universe, however, the Chameleon screening predicts a richer set of observational signatures that are detectable with astrophysical tests, because it is possible to have order unity violation of the macroscopic weak equivalence principle (WEP), i.e., extended objects do not fall at the same rate as in GR (Hui et al. 2009). In environments of low background $|\phi_{\mathrm{grav}}|$, objects with deep gravitational potential can self–screen, while those with shallow potential remain unscreened. For example, Jain & VanderPlas (2011) estimated that there could be up to $\sim 1\,\mathrm{kpc}$ separation of the stellar disk (composed of self–screened objects) from the dark matter and gas (both unscreened) inside unscreened dwarf galaxies, using orbital simulations under $f(R)$. In contrast, there is no analogous order one violation in the Vainshtein case, but the Vainshtein "spheres"[3] of individual objects interfere with each other. For example, in a two–body system where the separation is $\sim r_*$, the interference reduces the infall acceleration, and this reduction becomes most significant for two objects with equal masses (Belikov & Hu 2013).

The infall zone around clusters lies at the transition between the linear scale, where gravity is universally enhanced, and the local Universe where GR is frequently recovered, providing a unique avenue for distinguishing MG from GR. However, in both screening mechanisms the scalar ψ is coupled to density fluctuations via a nonlinear field equation, which can only be solved jointly with the matter field using numerical simulations. Lam et al.

Figure 1. *Top panel*: Halo mass functions in GR (solid), F5 (dotted), and F4 (dashed) simulations. *Bottom panel*: Fractional differences in halo mass function between the $f(R)$ simulations and the GR simulation. The shaded region in each panel indicates the mass scale where the halo catalogs are incomplete.

(2013) proposed a halo model-based approach to model the line-of-sight (LOS) velocity dispersions of galaxies in the infall region under both modified and normal gravities. In this study we hope to provide a complete picture of the coherent motions and distributions of galaxies around clusters in the two MG theories and their systematic deviations from GR, fully taking into account the non-linearities that are intrinsic to the Chameleon and Vainshtein mechanisms.

The GIK model of ZW13 describes the average galaxy infall in cluster–centric coordinates in terms of a 2D velocity distribution at each radius, comprising a virialized component with an isotropic Gaussian velocity distribution and an infall component described by a skewed 2D t-distribution with a characteristic infall velocity $v_{r,c}$ and separate radial and tangential dispersions. The virialized component is confined within a "shock radius" that is close to the virial radius of the cluster, so in the infall region (several to $20\,h^{-1}\mathrm{Mpc}$)[4] the GIK model reduces to a single infall component. ZW13 demonstrated that GIK profiles can be robustly recovered from the measurement of ξ_{cg}^s within the Millennium simulation (Springel 2005), and they applied the method to rich galaxy groups in the Sloan Digital Sky Survey (SDSS, York et al. 2000). In particular, the inferred $v_{r,c}$ profile provides a promising way of estimating the average dynamical mass of clusters and is likely insensitive to baryonic physics and galaxy bias (Zu et al. in prep). Although the ZW13 method is calibrated against GR simulations, we will show that the GIK model is also an excellent description of the infall behavior in MG simulations. Studies have shown that the peculiar velocities are more distinctively affected by modifications to gravity than the matter density field alone (Wyman & Khoury 2010; Jennings et al. 2012; Wyman et al. 2013; Li et al. 2013a),

---

[2] In practise, the functional form of $f(R)$ is tightly constrained by observations (Amendola et al. 2007; Amendola & Tsujikawa 2008).
[3] Strictly speaking, the Vainshtein mechanism works best for spherically symmetric sources, and not at all for planar sources; in reality, the screened region always has a complicated geometry that emerges from the geometry of the source.
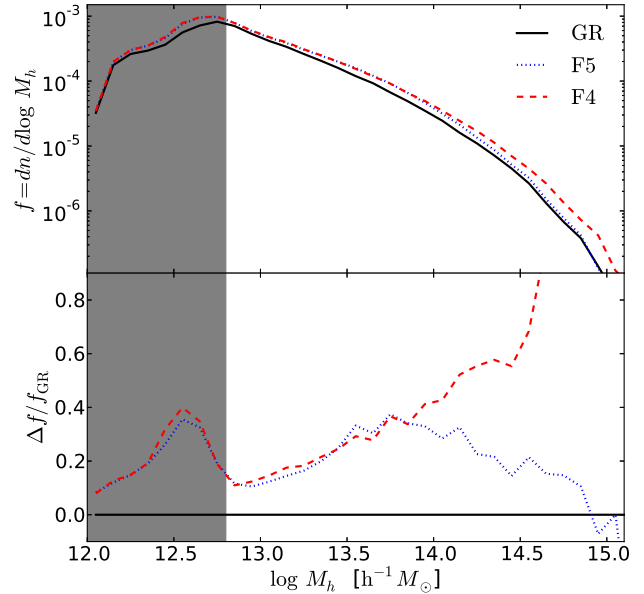
[4] Here $h \equiv H_0/100\,\mathrm{km\,s^{-1}\,Mpc^{-1}}$

and we expect the GIK to be a particularly acute test of MG theories and their screening mechanisms.

A virtue of using galaxy dynamics in the outskirts of clusters is that independent information on the average cluster mass profiles can be robustly extracted from stacked weak lensing (WL) experiments (Mandelbaum et al. 2006, 2009; Sheldon et al. 2009). Since photons do *not* respond to the extra scalar field,[5] lensing mass estimates will be different from dynamical mass estimates if gravity is modified from GR on relevant scales (Zhang et al. 2007; Reyes et al. 2010; Zhao et al. 2011b). However, implementing this test requires measuring mass profiles on scales where screening is inefficient, i.e., the cluster infall region rather than within the virial radius. For any given cluster sample detected by imaging, X-ray, or Sunyaev-Zel'dovich (SZ) experiments, one can either directly compare the average lensing mass and the GIK–estimated dynamical mass or search for inconsistency between the measured ξ_{cg}^s and the GIK–predicted ξ_{cg}^s using lensing mass estimates and assuming ΛCDM+GR. Alternatively, a simplified test can be performed when WL measurements are unavailable. Since any volume–limited cluster sample is thresholded by some mass observable (i.e., galaxy richness, X-ray luminosity, or SZ decrement) that correlates with the true mass (with some scatter), we can estimate the corresponding threshold in true mass using the abundance matching (AM) technique. However, the uncertainties of AM may be large when the scatter in the mass observable–true mass relation is large or/and the completeness of the cluster sample is low. For the sake of simplicity, in this paper we concentrate on the AM-based approach, and focus on cluster samples selected to have the same rank order in mass in the GR and MG simulations.

We present the results of GIK modelling of the Chameleon and Galileon simulations separately in the paper, as the two simulation sets were run with different initial conditions, cosmic expansion histories, and box sizes and resolution. We first introduce the Chameleon simulations in §2, including the specific $f(R)$ model, and halo statistics and kinematics. §3 presents the results of GIK modelling and the measurements of ξ_{cg}^s for the Chameleon clusters and compares that to GR. In §4, we presents a similar set of results for the Galileon clusters. We summarize and discuss the future prospects of our method in §5.

2 CHAMELEON SIMULATIONS

For the Chameleon modified gravity, we use a suite of large–volume $f(R)$ simulations ($1\,h^{-3}\mathrm{Gpc}^3$ box and 1024^3 particles) evolved with the N-body code ECOSMOG (Li et al. 2012a). The same set of simulations has been used to study the non-linear matter and velocity power spectra (Li et al. 2013a), redshift–space distortions (Jennings et al. 2012), and halo and void properties (Li et al. 2012b) in $f(R)$ gravity. The large volume of the simulations allows us to derive robust statistics from a large number of massive clusters ($M > 10^{14} h^{-1} M_\odot$). We do not make distinctions between the main halos and sub–halos, but include all the bound groups of particles identified by the spherical density halo finder AHF (Amiga's Halo Finder, Knollmann & Knebe 2009). The halo mass is defined by $M \equiv M_{\mathrm{vir}} = \Delta_{\mathrm{vir}} \rho_m V_{\mathrm{sphere}}(r_{\mathrm{vir}})$, where Δ_{vir} is the overdensity for virialized halos ($\Delta_{\mathrm{vir}} \simeq 276$ at $z = 0.25$ for typical ΛCDM cosmology; Bryan & Norman 1998) and ρ_m is the mean

[5] Though see Wyman 2011 for an interesting effect on lensing induced by MG
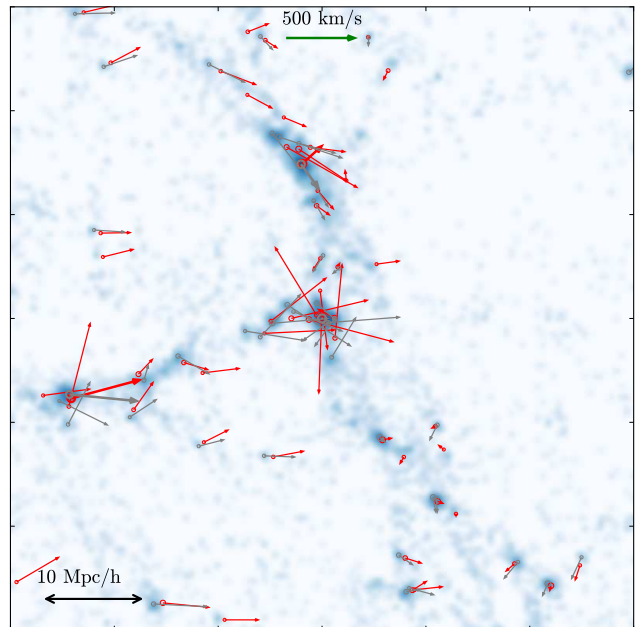
Figure 2. Positions and velocities (in cluster–centric frame) of halos around a massive cluster in the GR and F4 simulations. The dimension of the slice is $60\,h^{-1}\mathrm{Mpc} \times 60\,h^{-1}\mathrm{Mpc}$ with a thickness of $30\,h^{-1}\mathrm{Mpc}$, centered on a cluster of $M_h \sim 3.2 \times 10^{14}\,h^{-1} M_\odot$. The length of each arrow is v_{pec}/H_0, in units of $h^{-1}\mathrm{Mpc}$. The background grayscale shows the density field of the GR simulation. Gray and red arrows show the velocities of halos in the GR and F4 simulations, respectively, with larger circles and thicker arrows for halos of $M > 10^{14}\,h^{-1} M_\odot$.

density of the universe. We will briefly describe the $f(R)$ models here and refer the readers to Li et al. (2012a) for more details on the simulations.

The simulations adopt a specific $f(R)$ gravity model introduced by Hu & Sawicki (2007), with the functional form of $f(R)$ as

$$f(R) = -m^2 \frac{c_1 (R/m^2)^n}{c_2 (R/m^2)^n + 1}, \tag{1}$$

where the mass scale $m^2 \equiv H_0^2 \Omega_m$, c_1 and c_2 are dimensionless parameters, and n controls the sharpness of the transition of $f(R)$ from 0 in high–curvature limit ($R \to 0$) to $-m^2 c_1/c_2$ in low–curvature limit ($R \to \infty$). The corresponding scalar field in $f(R)$ theory is $\frac{df(R)}{dR}$, commonly denoted as f_R (i.e., the scalaron). Matching to the expansion history of flat ΛCDM universes (e.g., $\Omega_m = 0.24$ and $\Omega_\Lambda = 0.76$) requires a $R_0/m^2 \sim 41$ and a field value $f_{R0} \simeq -nc_1/c_2^2/(41)^{n+1} < 0$, where the subscript $_0$ represents the present day values. Therefore, the Hu & Sawicki model is effectively described by two parameters: n and f_{R0}. Models with $|f_{R0}| \lesssim 0.1$ are capable of evading solar system tests. For cosmological tests of Chameleon theories, models with $|f_{R0}| > 10^{-4}$ are ruled out by cluster abundance constraints from Schmidt et al. (2009b), and models with $|f_{R0}|$ below 10^{-6} are nearly indistinguishable from ΛCDM universes. We shall study two cosmologically interesting $f(R)$ models with $n = 1$ and $f_{R0} = -10^{-5}$, -10^{-4}, which will hereafter be referred to as F5 and F4, respectively. Jain et al. (2012) reported constraints of $|f_{R0}| < 10^{-7}$ from other astrophysical tests, so these models may no longer be observationally viable, but they nonetheless provide useful illustrations of MG effects and a natural comparison for the Vainshtein
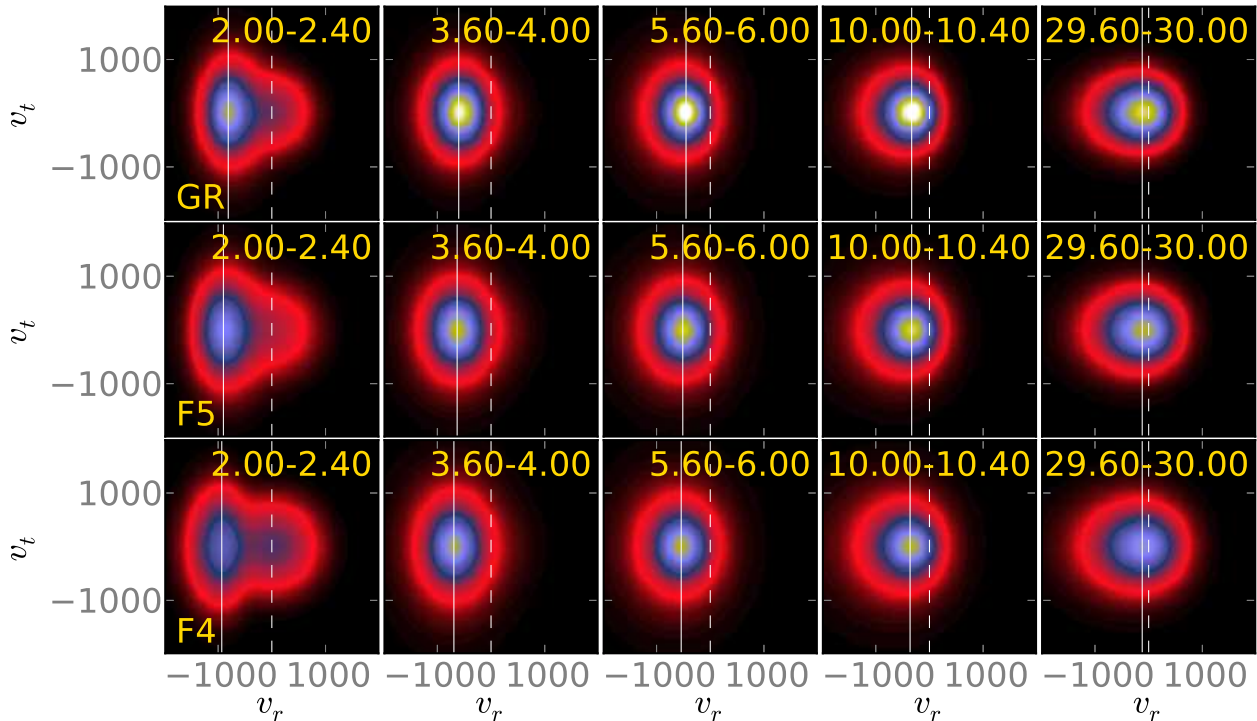
Figure 3. Joint probability distributions of radial and tangential velocities from the best fit to the GR (top), F5 (middle), F4 (bottom) simulations using our GIK model, in five different radial bins marked at the top of each panel (in units of $h^{-1}\mathrm{Mpc}$), for clusters of 1–$2 \times 10^{14}\,h^{-1}M_\odot$ in each simulation. In each panel, the vertical dashed line indicates the position of zero radial velocity while the solid line is the most probable radial velocity. The colour scales, indicating probability density in the (v_t, v_r) space, are identical across all panels (colourbars are thus not shown here).

screening model discussed later. The expansion history of the two $f(R)$ simulations is matched to one flat ΛCDM simulation that evolves from the same initial conditions under normal gravity with $\Omega_m = 0.24$, $\Omega_\Lambda = 0.76$, $h = 0.73$, and $\sigma_8 = 0.77$ (referred to as the "GR" simulation). The evolution of structure is the same in the three universes up to epochs around $z = 49$, which is the starting time of the simulations, since the fifth force in $f(R)$ gravity is vastly suppressed until then. By studying the time evolution of the matter and velocity divergence power spectra in $f(R)$, Li et al. (2013a) showed that different $f(R)$ models are in different stages of the same evolutionary path at any given time, and that varying the model parameter f_{R0} mainly varies the epoch marking the onset of the fifth force. The exact epoch of onset in each model depends on the scale of interest, i.e., at higher redshift for smaller scales (see figure 8 in Li et al. 2013a). We choose to focus on the $z = 0.25$ output of the simulations, mimicking the portion of the Universe most observed by existing and near–term future redshift surveys that contain large samples of clusters.

Figure 1 compares the halo mass functions from the GR, F5, and F4 simulations. The bottom panel shows the fractional enhancement of the halo mass function in the $f(R)$ simulations relative to the GR one. The shaded region ($M < M_{\mathrm{lim}} \equiv 6.4 \times 10^{12}\,h^{-1}M_\odot$) indicates the mass range where the halo catalogs are incomplete and the bumps in the shaded area of the bottom panel are likely due to numerical effects. Although sub–halos were included in the halo catalogs, at $M > M_{\mathrm{lim}}$ the halo mass functions are mostly contributed by main halos. The two $f(R)$ models predict very similar halo abundances below $6 \times 10^{13}\,h^{-1}M_\odot$, enhanced by 10–30% over the GR abundances. For halos in this mass range, the fifth force was activated early enough that the structure formation

has somehow converged in the two $f(R)$ models. However, on the high–mass end, the halo mass function in the F4 model shows even stronger enhancement over GR, while in the F5 model the number of halos becomes closer to the ΛCDM prediction with increasing mass. The divergence of the halo mass functions predicted by the two $f(R)$ models beyond $\sim 10^{14}h^{-1}M_\odot$ indicates that the fifth force only started affecting the formation of massive clusters recently in the F5 model, producing smaller enhancement in the halo abundance compared to F4. For some very massive clusters in the F5 model (e.g., see figure 3 in Li et al. 2012b), the gravitational potential has begun to dominate the background scalaron, activating the Chameleon mechanism to recover GR in the infall region, while in the F4 model the Chameleon screening likely never activates anywhere in the universe. Figure 1 is in good agreement with the study of Schmidt et al. (2009a), where a series of smaller but higher resolution $f(R)$ simulations are employed. Lombriser et al. (2013) modeled the halo mass functions measured from the same sets of $f(R)$ simulations using environment– and mass–dependent spherical collapse model in combination with excursion set theory.

With neither well–resolved sub–halos nor simulated galaxies in the simulations, the common prescription for constructing mock galaxy catalogs is through Halo Occupation Distributions (HODs, Jing et al. 1998; Peacock & Smith 2000; Seljak 2000; Scoccimarro et al. 2001; Berlind & Weinberg 2002; Zheng et al. 2005). However, the minimum required mass threshold for a complete halo sample in the Chameleon simulations, M_{lim}, is overly high for any meaningful HOD — galaxies similar to the Milky Way and M31 would be absent. Therefore, we simply use particles and halos as our proxies for galaxies in the paper, and the behavior of HOD galaxies should be intermediate between that of the "parti-
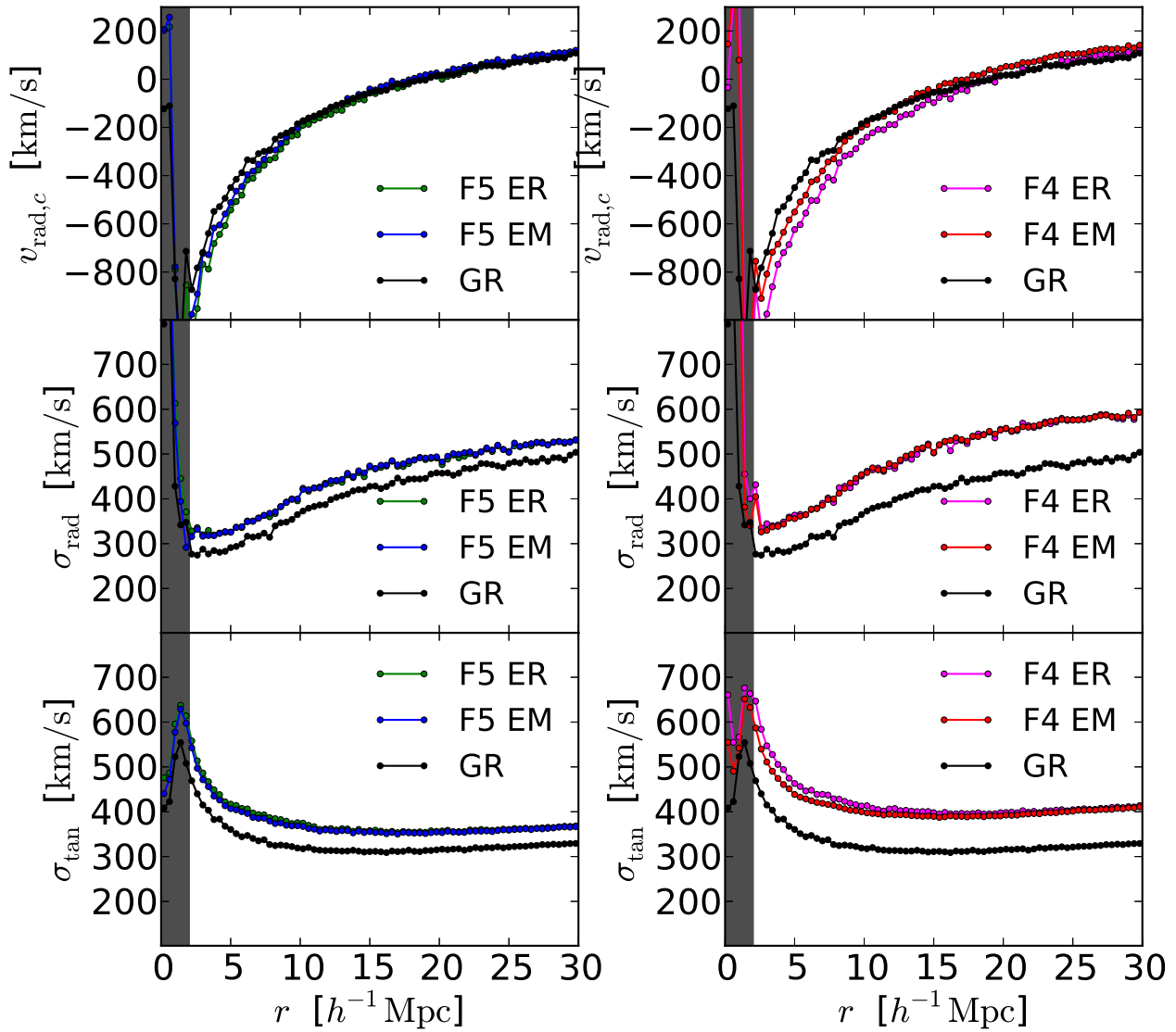
Figure 4. Best–fitting characteristic infall velocity (top), radial velocity dispersion (middle), and tangential velocity dispersion (bottom) as functions of radius. Left and right columns compare the results of F5 and F4 simulations to that of GR, respectively. The shaded region in each panel indicates the scales below the maximum infall radius, where the GIK measurements are less robust. Halos in the $f(R)$ simulations are selected as either having equal mass (EM) or equal rank order (ER) to the halos of $1 - 2 \times 10^{14} h^{-1} M_\odot$ in the GR simulations. See text for details.

cle" galaxies and "halo" galaxies. Since we are focused on the relative behavior of MG and GR simulations, the impact of choices for galaxy proxy on our conclusions should be small. We will usually refer simply to "galaxies", when it is clear from context whether we are using particles or halos as our proxies.

Before going into the statistical properties of galaxy infall, we hope to gain some intuitive understanding of the differences in infall between MG and GR by looking at Figure 2. Taking advantage of the same initial condition shared by the $f(R)$ and GR simulations, we locate at the frame center two primary clusters ($M \sim 3.2 \times 10^{14} h^{-1} M_\odot$) at $z = 0.25$ that formed from the same seed in the initial density fluctuation field in the F4 (red, for which the fifth force is stronger) and GR (gray) simulations, respectively, and plot all halos with mass above $6 \times 10^{12} h^{-1} M_\odot$ as circles, with their relative velocities to the primary cluster indicated by the arrows. The dark matter density field in the GR simulation

is illustrated by the grayscale background, highlighting the three filamentary structures that funnel the infalling halos. The radius of each circle is proportional to the halo mass, with the thick ones representing halos more massive than $10^{14} h^{-1} M_\odot$. The length of each arrow is $v_{\rm pec}/H_0$, corresponding to the redshift–space displacement (in units of $h^{-1}{\rm Mpc}$) that would be seen by a distant observer aligned with the velocity vector. Figure 2 shows that the GIK around *individual* clusters is highly anisotropic, and while the difference in the spatial distribution between GR and F4 halos is irregular and fairly mild, it is somewhat enhanced in redshift space. To avoid clutter, we do not show halos from the F5 model, which should display smaller differences from GR because of its smaller impact from the fifth force. In the next section, we will show that by stacking individual frames like Figure 2 for clusters of similar mass, the anisotropy goes away and the average infall kinematics can be well described by the GIK model proposed in ZW13,
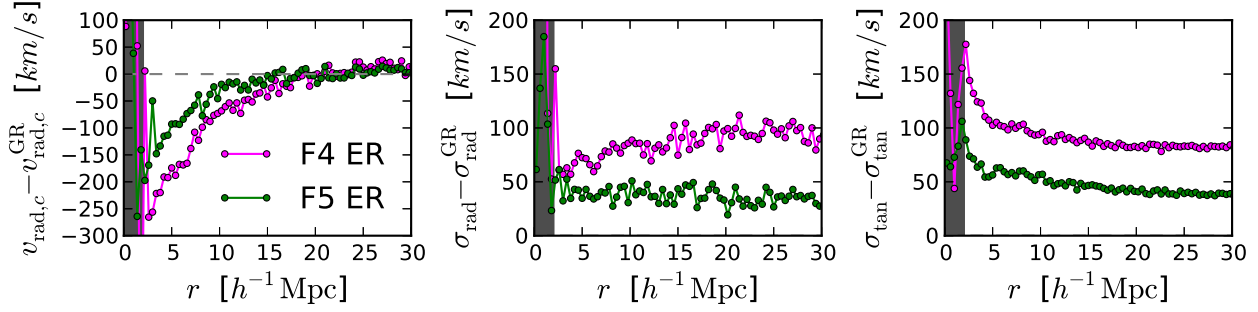
Figure 5. Difference in GIK profiles between the $f(R)$ and GR simulations, using clusters of equal rank–order (ER).

for both the $f(R)$ and ΛCDM models. More importantly, the enhanced difference in the redshift space between MG and GR models can be captured by systematic differences in the parameters of the GIK model, namely, the characteristic infall velocity $v_{r,c}$, the radial velocity dispersion $\sigma_{\rm rad}$, and the tangential velocity dispersion $\sigma_{\rm tan}$.

3   GALAXY INFALL KINEMATICS

The halo mass functions in Figure 1 suggest that the fifth force became unscreened earlier in F4 than in F5, which gives it more time to affect the velocity field in the former. As a result, at $z = 0.25$ clusters in both the F4 and F5 models should exhibit more enhanced galaxy infall compared to GR, but we expect the enhancement to be more substantial in the F4 model. For the small number of screened clusters in the F5 model, the infalling galaxies around Chameleon clusters should feel similar instantaneous accelerations as their counterparts around similar clusters in GR. However, the peculiar velocities of galaxies were enhanced by the fifth force when they were further away from the clusters. By the time they reached to the screened region, the peculiar velocities were already higher, so the infall stays stronger even though the underlying gravity recovers to GR. Our goal here is to quantify this modification to galaxy infall induced by $f(R)$ gravities as function of f_{R0} within the framework of GIK modelling.

To compare the average GIK among the three simulations, we select dark matter halos with $M_{\rm vir} \in 1\text{--}2 \times 10^{14}\,h^{-1}M_\odot$ in the ΛCDM simulation as our fiducial GR cluster sample, and those with the same mass range in the $f(R)$ simulations as the "equal–mass" (EM) cluster samples. As mentioned in the introduction, we also select specific halo samples in the $f(R)$ simulations to have the same rank–order in mass as the fiducial GR clusters, i.e., the "equal–rank" (ER) cluster samples. The ER clusters generally have slightly larger masses than the EM ones, with $1.13\text{--}2.14 \times 10^{14}\,h^{-1}M_\odot$ and $1.27\text{--}2.52 \times 10^{14}\,h^{-1}M_\odot$ in F5 and F4 models, respectively. The ER sample thus resembles the set of clusters that formed from the same initial density peaks as the fiducial GR ones. In the limit of very rare, highly biased peaks, the large–scale cluster bias b_c, defined by the ratio between the cluster–matter correlation function and the matter auto–correlation ξ_{cm}/ξ_{mm}, is $\propto \sigma_8^{-1}$, yielding $\xi_{cm} \propto \sigma_8$ on large scales. Operationally, the EM comparison would be most relevant to an observational study of clusters whose virial masses are calibrated by WL (and thus accurate in both GR and MG). Alternatively, if one ranks clusters by a mass proxy such as galaxy richness, X–ray luminosity, or SZ signal, then selects clusters above a threshold (i.e., AM

method), the ER comparison is more relevant. Hereafter we simply denote the fiducial GR sample as "GR" while comparing it to the "EM" and "ER" samples in MG simulations.

3.1   Velocity Field Model

As mentioned in the introduction, the two–component GIK model is an excellent analytic description of the joint 2D distribution of radial and tangential velocities of galaxies in the cluster–centric frame, $P(v_r, v_t)$. Here we will present the results of GIK modelling for the cluster samples defined above, and refer the readers to ZW13 for details on the GIK parameterization and fitting procedures.

Figure 3 shows the best–fitting $P(v_r, v_t)$ for the GR (top), F5–EM (middle), and F4–EM (bottom) cluster samples at five different radial bins, using dark matter particles as proxy for galaxies. Negative v_r indicates falling toward clusters. Following ZW13, we define v_t as the tangential velocity component that is projected in the plane of LOS axis and galaxy position vector in the cluster–centric frame (see the 3D diagram in the figure 2 of ZW13). Since the *average* galaxy motion around the cluster center is isotropic, the probability distribution of v_t is symmetric about zero. Hereafter we refer to v_t simply as the "tangential velocity". Note that the Hubble flow is subtracted when defining v_r, but it will be incorporated when modelling ξ_{cg}^s. The GIK of the three cluster samples in Figure 3 show some generic trends with radius: 1) The distribution has two distinct components on very small scales (leftmost column) but only shows a single infall component on large scales; 2) the infall component is symmetric about the mean v_r near the turn–around radius, where infall velocity is comparable to Hubble flow (middle column); 3) the v_r distribution of the infall component is skewed toward positive velocities beyond the turn–around radius (two right columns), but is negatively skewed below that radius (two left columns).

The impacts of modified gravity on $P(v_r, v_t)$ are subtle but nonetheless visually apparent in Figure 3 when comparing the three models at the same radial bin (i.e., within the same column). The solid vertical line in each panel indicates the most probable radial velocity, which shifts to more negative v_r with increasing $|f_{R0}|$ (i.e., from top to bottom) at each radius. Simultaneously, the dispersions of the infall component in the radial and tangential directions also increase as function of f_{R0} — the joint distributions in the F4 model are more extended than in GR. This increased width results in the decreased peak amplitude of the distributions (which are normalized to unity by definition).
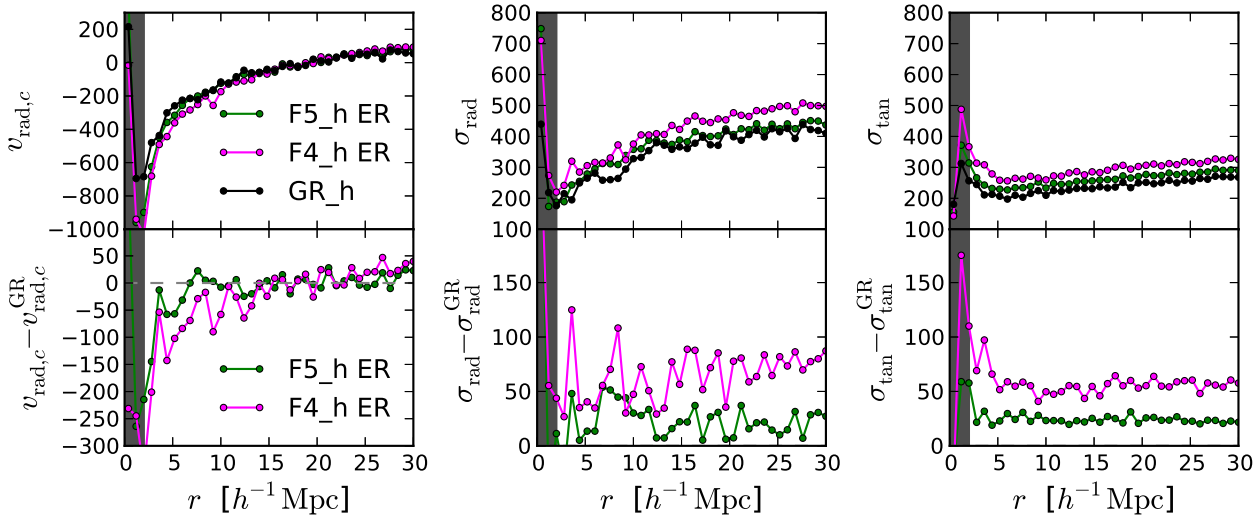
To quantify the differences in GIK among the three simula-

Figure 6. Comparison of GIK profiles in the GR, F5, and F4 simulations, using halos as proxy for galaxies instead of dark matter particles as in Figures 4 and 5.

tions, we will focus on the impacts of modified gravity on three of the GIK parameters ($v_{r,c}$, $\sigma_{\rm rad}$, and $\sigma_{\rm tan}$). We ignore the other GIK parameters defined by ZW13 (seven in total), including two parameters describing the virialized component that are irrelevant to this paper, and two others that describe the skewness and the kurtosis of the infall component, which we found to be insensitive to modified gravity. Note that the characteristic radial velocity $v_{r,c}$ is not the mean, median, or mode of the radial velocity distribution, but is a characteristic velocity naturally associated with the definition of the skewed t-distribution used for describing the GIK infall component (see ZW13, equation 6).

Figure 4 presents the best–fit GIK parameters as functions of radius for the F5 (left) and the F4 (right) models, respectively. In each panel we show the parameter profiles for all three types of cluster samples (GR, EM, and ER). The shaded region in each panel indicates the radial bins where GIK is dominated by the virialized component and the fit to the infall component is less robust. For the F5 model, the halo mass function is close to that of ΛCDM at high masses, so the EM and ER samples have little difference in mass and their GIK profiles look very similar. However, as expected from Figure 3, the two F5 cluster samples in the $f(R)$ simulation show stronger infall (top left) and larger velocity dispersions (center and bottom left) compared to the GR sample. For the F4 model, the difference between the EM and ER samples is larger, especially in the $v_{r,c}$ profiles (top right), where the difference between the ER and GR profiles is almost double that between the EM and GR ones. For both samples, the F4 results are more easily distinguished from GR than the F5 results, as expected. Since we anticipate that ER comparisons will be more observationally relevant in most cases, we will focus henceforth on the GIK of ER cluster samples in the MG simulations.

We highlight the differences in GIK profiles between ER and GR clusters for both Chameleon models in Figure 5. The characteristic infall velocity profiles exhibit significant effects from the Chameleon gravity on scales below $15\,h^{-1}{\rm Mpc}$, showing $\sim 100\,{\rm km/s}$ and $200\,{\rm km/s}$ enhancement at $5h^{-1}{\rm Mpc}$ for the F5 and F4 models, respectively. Beyond $15\,h^{-1}{\rm Mpc}$ the $v_{r,c}$ profiles converge to the GR prediction. The dispersion profiles in $f(R)$ models deviate from GR on all distance scales, with the differences almost

constant and decreasing with radius for $\sigma_{\rm rad}$ and $\sigma_{\rm tan}$, respectively. The magnitude of the deviations we see here is very encouraging — $\sim 100\,{\rm km/s}$ difference in both the $v_{r,c}$ and the dispersions is already detectable within 2σ in ZW13, where a preliminary GIK constraint is obtained using two samples of SDSS rich groups (with group number ~ 2000 and ~ 600, respectively) and the SDSS DR7 main galaxy sample.

Using dark matter particles as proxy for galaxies effectively assumes that galaxies have the same density profile and velocity distribution as dark matter particles within halos. In reality, we expect central galaxies to have low peculiar velocities relative to the halo center of mass, and the spatial distribution may be less concentrated than the matter (see, e.g., Budzynski et al. 2012). To bracket the expectations for constraining GIK using realistic galaxy samples, we repeat the above experiment using halos instead of particles as proxy for galaxies. This mimics the scenario where a Luminous Red Galaxy (LRG, Eisenstein et al. 2001) galaxy sample is employed, implying approximately one galaxy per halo as one extreme of the HOD (Zheng et al. 2009). Figure 6 summarizes the result of this experiment. We denote the curves correspondingly as "GR_h", "F5_h", and "F4_h" in the figure. The GIK profiles are much noisier because of the rarity of halos, but the differences among the three samples are similar to those seen in Figure 5, but smaller in magnitude by about a factor of two. We infer that the difference in GIK seen in Figure 5 using "particle" galaxies has approximately equal contributions from two sources, Chameleon modifications to the random motions within halos (i.e., "'1-halo") and the impact of Chameleon gravity on the bulk inflow of halos (i.e., "'2-halo"). Quantitative predictions for a particular galaxy sample will require simulations that resolve the host halos and thus allow a full HOD model of the population, incorporating both 1-halo and 2-halo effects with appropriate weight.

3.2 Cluster–galaxy Correlation Function

The redshift–space cluster–galaxy cross–correlation function, ξ^s_{cg}, is a comprehensive characterization of the statistical relation between clusters and galaxies, influenced by both the real–space cross–correlation ξ^r_{cg} and the peculiar velocities induced by the
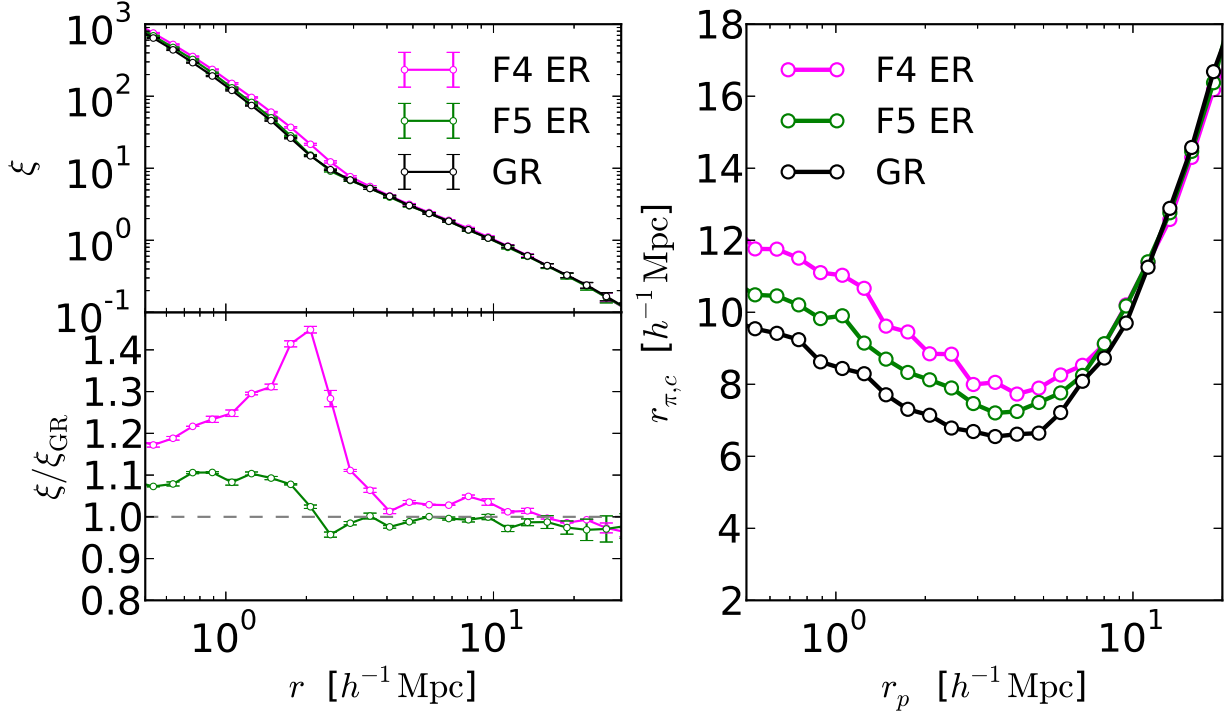
Figure 7. *Left Panel*: Comparison of real–space correlation functions in the GR, F5, and F4 simulations, using particles as proxy for galaxies. *Right Panel*: Characteristic LOS distances derived from the redshift–space correlation functions in Fig. 8.

cluster gravitational potential. Mathematically, $\xi^s_{cg}(r_p, r_\pi)$, a function of projected cluster–galaxy separation r_p and line-of-sight redshift separation r_π, can be derived by convolving the real–space $\xi^r_{cg}(r)$ with the Hubble flow–corrected LOS velocity distribution, which can be straightforwardly predicted from the GIK model (see equation 11 in ZW13). ZW13 demonstrated that the GIK can be extracted from the observed ξ^s_{cg}, by taking advantage of the non–degenerate imprint of each GIK element on the 2D pattern of ξ^s_{cg}. In this section we will examine the impact of Chameleon gravity on the real and redshift–space cluster–galaxy correlation functions in the $f(R)$ simulations, using particles as proxy for galaxies.

For measuring ξ^r_{cg}, we count the numbers of particles around clusters in spherical shells of successive radii, ranging from $100\,h^{-1}\mathrm{kpc}$ to $30\,h^{-1}\mathrm{Mpc}$ with logarithmic intervals, then average over all clusters in each bin and normalize by the particle numbers expected in a randomly located shell of equal volume. We measure ξ^s_{cg} in a similar way, counting galaxies in cylindrical rings of successive LOS distance r_π for each projected separation r_p (assuming a distant–observer approximation so that the LOS is an axis of the box). Uncertainties in both measurements are estimated by Jackknife re–sampling the octants of each simulation box.

We start by showing the real–space cluster–galaxy correlation function ξ^r_{cg} for the GR, F4–ER, and F5–ER cluster samples in the left panels of Figure 7. In the top left panel, all three correlation functions exhibit a break at $2-3\,h^{-1}\mathrm{Mpc}$, marking the transition from the NFW–like density distribution (Navarro et al. 1997) within halos to a biased version of the matter auto–correlation function on large scales (Hayashi & White 2008; Zu et al. 2012). The bottom left panel shows the ratio of ξ^r_{cg} between the ER samples in $f(R)$ simulations and the GR sample. On scales below the break radius, ξ^r_{cg} of the ER clusters show enhancement of 10% and 20% in the F5 and F4 models, respectively, because they are intrinsically

more massive than their counterparts in the ΛCDM simulation. On scales larger than $\sim 5\,h^{-1}\mathrm{Mpc}$, the ER clusters have nearly the same large–scale clustering as the GR sample. Since we are measuring the cross–correlation with dark matter particles, these ξ^r_{cg} profiles also determine the cluster–galaxy WL profile (see, e.g., eq. 13 of Zu et al. 2012).

On intermediate scales, there is a bump at $\sim 2\,h^{-1}\mathrm{Mpc}$ in the ratio between ξ^r_{cg} of the F4–ER and the GR samples, but not in the ratio curve for F5–ER. In the F4 model, the fifth force became unscreened from quite early time, so that the velocity field has been enhanced for a long time by $z = 0.25$. This means that the peculiar velocities are enhanced by roughly the same factor κ as the gravitational force, where κ is between unity and $4/3$, and the kinetic energy of particles in F4 is thus κ^2 times that in GR; meanwhile, the gravitational potential in F4 is $\sim \kappa$ times as deep as in GR. The net result is that the MG effect on the particle kinetic energy dominates over its effect on the cluster potential, so that as a compromise the particles tend to move toward the outer parts of clusters. The situation is different in the F5 model, where the fifth force became unscreened quite late. By $z = 0.25$, the fifth force has become unscreened but only for a short period, so that particle velocities have not been significantly affected by it. On the other hand, due to the disappearance of the screening, the potential of the cluster suddenly became deeper. The result is a stronger MG effect on the potential than on the kinetic energy of particles, and particles tend to move toward the inner parts of clusters. These features have been observed in the halo density profiles of $f(R)$ simulations before (e.g., Zhao et al. 2011a), and similar ones have been found in coupled quintessence simulations. Using cluster WL measurements, Lombriser et al. (2012) exploited this small–scale enhancement of cluster density profiles in Chameleon gravity and
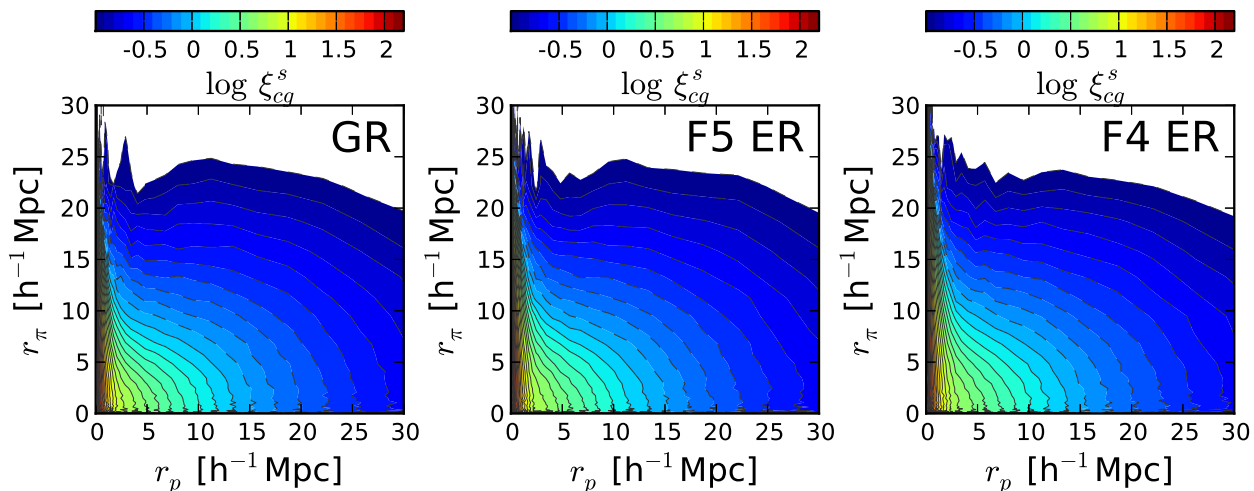
Figure 8. Redshift–space correlation functions in the GR, F5, and F4 simulations.

obtained a constraint of $|f_{R0}| < 3.5 \times 10^{-3}$ at 95% confidence level.

Figure 8 presents the redshift–space cluster–galaxy correlation functions for the three cluster samples, showing a stronger small–scale Fingers-of-God (FOG, Jackson 1972) effect with increasing $|f_{R0}|$, but with similar LOS squashing effect on large scales (a.k.a., Kaiser effect, Kaiser 1987). However, the most easily visible features of ξ_{cg}^s in Figure 8 are driven by the radial gradient of cluster density profiles, which are fairly insensitive to the influence of Chameleon modifications to gravity according to the left panel of Figure 7. Modified gravity also changes the shape of ξ_{cg}^s at fixed r_p via its effects on the GIK, re–distributing matter/galaxies along the r_π axis. To reveal this LOS distortion of ξ_{cg}^s by $f(R)$, following ZW13, we compute the characteristic LOS distance $r_{\pi,c}(r_p)$ by fitting a powered exponential function to ξ_{cg}^s at each fixed r_p,

$$\xi_{cg}^s(r_p, r_\pi) \simeq \xi_{cg}^s(r_p, r_\pi = 0) \exp\left\{-\left|\frac{r_\pi}{r_{\pi,c}}\right|^\beta\right\}, \quad (2)$$

where $r_{\pi,c}$ is the characteristic length scale at which ξ_{cg}^s drops to $1/e$ of its maximum value at $r_\pi = 0$. The shape parameter β yields a Gaussian cutoff for $\beta = 2$ and simple exponential for $\beta = 1$, though any value is allowed in the fit. The results of this fitting are shown in the right panel of Figure 7. The $r_{\pi,c}$ vs. r_p curves exhibit the characteristic U-shape discovered in ZW13 — FOG stretching at small r_p gives way to Kaiser compression at intermediate r_p which gives way to Hubble flow expansion at large r_p. Clearly, the ξ_{cg}^s distribution along the LOS is a sensitive probe of $f(R)$ models at $r_p < 6\,h^{-1}\mathrm{Mpc}$, becoming more extended with increasing $|f_{R0}|$ (e.g., $r_{\pi,c} = 7$, 8, and $9\,h^{-1}\mathrm{Mpc}$ at $r_p = 2\,h^{-1}\mathrm{Mpc}$ for GR, F5, and F4 models, respectively).

The detailed shape of $\xi_{cg}^s(r_p, r_\pi)$ reflects a complex interplay among the four elements of the galaxy kinematics around clusters, including the three GIK profiles of the infall component ($v_{r,c}$, σ_{rad}, and σ_{tan}) and the virial component (see figure 10 of ZW13 for an illustrative experiment). For the same reason, the increase of $r_{\pi,c}$ with f_{R0} has different origins at different projected distances. Below $r_p \sim 1.5\,h^{-1}\mathrm{Mpc}$, the response of $r_{\pi,c}$ to f_{R0} is uniform with r_p, caused by the uniform increase of dispersion in virial motions. For $r_p \sim 1.5 - 3\,h^{-1}\mathrm{Mpc}$, the f_{R0} dependence of $r_{\pi,c}$ has two contributing sources, one being the increase of tan-

gential velocity dispersions, the other the increase of maximum infall velocities, which transport high–speed matter/galaxies from one side of the cluster in real space to the opposite side in red-shift space (i.e., the portion of the FOG effect caused by infall). For $r_p \sim 3 - 6\,h^{-1}\mathrm{Mpc}$, f_{R0} influences the $r_{\pi,c}$ profile mainly via the increase of tangential velocity dispersions. The radial velocity dispersions only enter into play at large r_p, where the diagnostic power of ξ_{cg}^s is diminishing.

4 RESULTS FOR A GALILEON MODEL

Although Chameleon theories like the Hu & Sawicki $f(R)$ model include the phenomenology of ΛCDM without a *true* cosmological constant, Wang et al. (2012) proved that the theories that invoke a Chameleon–like scalar to explain cosmic acceleration essentially rely on a form of dark energy rather than a genuine MG effect,[6] even if they are initially described in terms of an altered gravitational action. Conversely, the Galileon class of theories is capable of accelerating the cosmic expansion even in the absence of any form of dark energy (e.g., de Rham et al. 2011a; Gratia et al. 2012; Appleby & Linder 2012; Barreira et al. 2012), i.e., they have so–called "self–accelerating" solutions. Here we study the GIK for a simplified version of such kind of Galileon theories, where an extra Galileon–type scalar field that manifests the Vainshtein mechanism permeates a universe with the ΛCDM background cosmology.

We employ a suite of Galileon simulations with 512^3 particles on a 512^3 grid of $L_{\mathrm{box}} = 400\,h^{-1}\mathrm{Mpc}$, evolved using the Particle Mesh code of Khoury & Wyman (2009), which was updated by Wyman et al. (2013) (for other Galileon/DGP simulations, see, e.g., Chan & Scoccimarro 2009; Schmidt 2009; Li et al. 2013b; Barreira et al. 2013). The simulations were first used by Wyman et al. (2013) for studying the statistics of matter clustering in real and redshift spaces. We will briefly introduce the Galileon implementation and parameterization here and refer the readers to Wyman et al. (2013) for details.

---

[6] For a "genuine" MG effect, the cosmic acceleration should stem entirely from the conformal transformation from the Einstein frame to the Jordan frame. See Wang et al. (2012) for details.
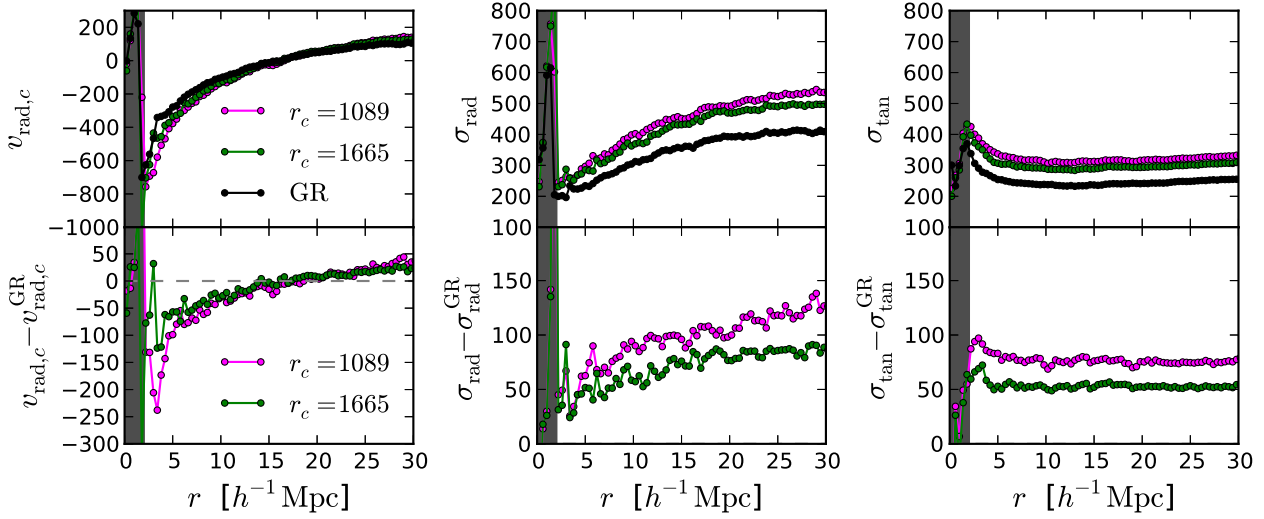
Figure 9. Similar to Figure 6, but for the Galileon simulations and using particles as proxy for galaxies, around clusters of equal rank order (ER).

As described in the introduction, the Vainshtein mechanism has only one parameter, r_c, which is interpreted as the Compton wavelength associated with the graviton mass in massive gravity theories, so that the Vainshtein radius of a point mass with mass M is

$$r_*^p \equiv (r_s r_c^2)^{\frac{1}{3}} \simeq 2.1 \left(\frac{M}{10^{14} M_\odot} \right)^{\frac{1}{3}} \left(\frac{r_c}{10^3 \mathrm{Mpc}} \right)^{\frac{2}{3}} \mathrm{Mpc}. \quad (3)$$

For extended objects of the same mass M, the Vainshtein radii are generally several times larger than $r_*^p(M)$ — e.g., a NFW halo with $M = 10^{14} M_\odot$ has $r_* \sim 10\,\mathrm{Mpc}$, and galaxies generally have $r_* \sim 1\,\mathrm{Mpc}$. Therefore, whereas the cluster interior below the virial radius belongs to the strongly Vainshtein–screened regime, the cluster infall region is weakly screened, displaying complex interference among Galileon fields sourced by the primary cluster and the infalling galaxies and galaxy groups.

We make use of three simulations with the same expansion history and initial condition, one of them a flat ΛCDM universe evolved under normal gravity with $\Omega_m = 0.24$, $\Omega_\Lambda = 0.76$, $h = 0.73$, and $\sigma_8 = 0.80$, and the other two immersed in Galileon scalar fields with $r_c = 1665$ and $1089\,\mathrm{Mpc}$. In the figures we refer to them simply as "GR" (i.e., $r_c = +\infty$), $r_c = 1665$, and $r_c = 1089$, respectively, and a smaller r_c implies an earlier onset of the fifth force and an effectively stronger fifth force in the late Universe (see, e.g., figure 5 of Wyman et al. 2013, for the change of linear growth rate as function of r_c). Note that the "GR" simulation is different from what we used for comparing to the $f(R)$ simulations, albeit with similar cosmology. Dark matter halos are identified via a spherical overdensity finder with the halo mass defined by $M \equiv M_{200} = \Delta_{200} \rho_m V_{\mathrm{sphere}}(r_{200})$, different from the M_{vir} used for the Chameleon simulations. Since $\Delta_{200} < \Delta_{\mathrm{vir}}$, a halo would have a higher M_{200} than M_{vir} (e.g., $M_{200} \sim 1.1 \times M_{\mathrm{vir}}$ for a $10^{14} h^{-1} M_\odot$ cluster at $z = 0.25$ in ΛCDM). The halo mass functions, halo bias functions, and matter power spectra of the three simulations can be found in Wyman et al. (2013). Targeting the same redshift range as in §2, we use the $z = 0.20$ output of the simulations (not $z = 0.25$ due to the different sets of recorded epochs in the two suites of simulations).

Since the volume of the Galileon simulations is only 6.4% of that of the Chameleon simulations, we have to select samples

with a wider mass bin size for robust GIK measurements. For the fiducial cluster sample in the GR simulation we include clusters with $M_{200} \in 1$–$3 \times 10^{14} h^{-1} M_\odot$, and similar to §2 we also select two ER cluster samples from respective Galileon simulations, with $M_{200} \in 1.15$–$3.52 \times 10^{14} h^{-1} M_\odot$ and $M_{200} \in 1.23$–$3.87 \times 10^{14} h^{-1} M_\odot$ in the $r_c = 1665$ and $r_c = 1089$ models, respectively. Unlike §2, we do not show the results from the EM cluster samples for the GR vs. Galileon comparisons, as the relative difference between the EM and ER samples is similar to what we see in the Chameleon simulations. Because of the smaller volume, we can only afford to use dark matter particles as proxy for galaxies. Note that the Galileon cluster sample here comprises halos that are intrinsically smaller than the one used in §2, due to different overdensity thresholds used in mass definitions.

Figure 9 compares the GIK profiles of the two ER samples in the Galileon simulations to that of the fiducial GR cluster sample. As intrinsically less massive systems, the fiducial GR clusters show weaker infall velocities and velocity dispersions than the GR clusters used in the Chameleon comparison at all distances (e.g., comparing the black curves in the top panels of Figure 9 to the black curves in Figure 4). However, the relative difference between the MG and GR samples overall looks very similar to what we see in the Chameleon comparison (e.g., comparing the bottom panels of Figure 9 to Figure 5). As expected, $v_{r,c}$, σ_{rad}, and σ_{tan} all become stronger with decreasing r_c (i.e., stronger fifth force). Specifically, $v_{r,c}$ shows ~ 50 and $100\,\mathrm{km/s}$ enhancement at $r = 5 h^{-1}\mathrm{Mpc}$ for the $r_c = 1665$ and $r_c = 1089$ models, respectively, which are comparable to the fractional enhancements in the F5 and F4 Chameleon models, respectively.

The only major difference between Figure 9 and Figure 5 appears in the bottom middle panel: The deviation of σ_{rad} profiles from the GR prediction decreases as function of distance, from $125/90\,\mathrm{km/s}$ at $r = 30 h^{-1}\mathrm{Mpc}$ to $60/50\,\mathrm{km/s}$ at $r = 5 h^{-1}\mathrm{Mpc}$, whereas in the Chameleon comparison the deviation of σ_{rad} stays more or less constant with distance. This difference in σ_{rad} may be reflecting the different ranges of fifth force in the two models: the Galileon has infinite range, so the force is enhanced further way from clusters, whereas the Chameleon force is Yukawa–suppressed on large scales. However, the pattern of ξ_{cg}^s is insensi-

tive to $\sigma_{\rm rad}$ at $r_p < 6\,h^{-1}\mathrm{Mpc}$ where the ξ^s_{cg} measurement is the most robust, making it an unpromising tool for distinguishing the two mechanisms. The GIK profiles of the EM cluster samples in the Galileon simulations closely follow those of their corresponding ER counterparts, albeit with slightly weaker amplitudes.

Figure 10 compares the real–space cluster–galaxy cross–correlation function ξ^r_{cg} (left) and the characteristic LOS distance $r_{\pi,c}$ (right) measured for the three cluster samples. The shaded region indicates the scales below the force softening length of the simulations, where the correlation function and velocity dispersions are artificially suppressed. On small scales, the ratios between ξ^r_{cg} of the Galileon ER samples and fiducial GR sample (bottom left) display similar features to these in Figure 7, including an enhancement interior to the virial radius because the ER clusters are more massive, and a bump around $2\,h^{-1}\mathrm{Mpc}$, though this is only $\sim 1.2\,h^{-1}\mathrm{Mpc}$ away from the force resolution limit. To check whether the bump is a numerical artefact, we repeated the same measurements of ξ^r_{cg} using a suite of higher resolution (but smaller volume) Galileon simulations and verified that the bump is physical. Similar to the $f(R)$ case in the F4 model, the fast transition from Galileon force outside to normal gravity inside causes a sudden change of the depth of the potential well, but not the galaxy velocity (or kinetic energy), which has been experiencing enhancement well before infall. As the galaxies have excessive kinetic energy, they tend to move to the outer parts of halos, making the density profile lower in the central region of clusters and higher near the edges.

On large scales, the ER samples in the Galileon simulations exhibit stronger clustering than the GR clusters. This enhancement in ξ^r_{cg} can be understood by starting from the findings of Wyman et al. (2013), which suggest that the halo mass function, the halo bias function, and the matter power spectrum of the Galileon simulations are like those of ΛCDM universes with higher σ_8.[7] For example, at $z = 0$ the $r_c = 1665$ and the $r_c = 1089$ simulations resemble the ΛCDM universes with $\sigma_8 = 0.88$ and $\sigma_8 = 0.92$, respectively. Since the large–scale ξ^r_{cg} of ER clusters is almost linearly proportional to the effective σ_8, we observe $\sim 10\%$ and 15% enhancement in ξ^r_{cg} at $\sim 10\,h^{-1}\mathrm{Mpc}$ for clusters in the $r_c = 1665$ and $r_c = 1089$ models, respectively.

For the redshift–space cluster–galaxy cross–correlation function, because the impact of the Galileon field on GIK is similar to that in the Chameleon models, the $r_{\pi,c}$ curves in Galileon simulations also exhibit similar deviations from the GR curves, as shown in the right panel of Figure 10. The lack of upturn of $r_{\pi,c}$ at small r_p is a consequence of force resolution suppressing velocity dispersions; we expect that simulations with higher force resolution would show the characteristic U-shape for all three models. The overall lower amplitude of $r_{\pi,c}$ compared to Figure 7 is again the result of selecting intrinsically less massive halos. When we select the Galileon clusters to have equal–mass to the GR clusters, the enhancement in large–scale clustering (left panel) disappears because the large–scale bias is steep function of mass, but the differences in GIK and $r_{\pi,c}$ remain.

---

[7] Though they can be distinguished from ΛCDM by examining the Kaiser effect, where changing σ_8 cannot mimic the large scale boost in the redshift–space clustering due to MG. See Wyman et al. (2013) for details.

5 CONCLUSIONS

We have investigated the impact of modified gravity on the galaxy infall motion around massive clusters by applying the GIK model developed in ZW13 to two suites of $f(R)$ and Galileon N-body simulations. Both MG theories seek to explain cosmic acceleration by modifying GR on cosmological scales, but they recover GR in dense regions via two distinct "screening" effects: the potential–driven Chameleon mechanism in $f(R)$ and the density–driven Vainshtein mechanism in Galileon. However, within the range of parameter space probed by our simulations (i.e., $10^{-5} \leqslant |f_{R0}| \leqslant 10^{-4}$ for $f(R)$ and $1089\,\mathrm{Mpc} \leqslant r_c \leqslant 1665\,\mathrm{Mpc}$ for Galileon), despite having quite different cosmic growth histories, the two theories exhibit strikingly similar GIK deviations from GR, with ~ 100–$200\,\mathrm{km/s}$ enhancement in the characteristic infall velocity at $r = 5\,h^{-1}\mathrm{Mpc}$, and ~ 50–$100\,\mathrm{km/s}$ broadening in the radial and tangential velocity dispersions across the infall region, for clusters with mass $\sim 10^{14}\,h^{-1}M_\odot$ at $z = 0.25$. These deviations are detectable through GIK modelling of the redshift–space cluster–galaxy correlation function ξ^s_{cg}, especially when combined with cluster WL measurements. We highlight the imprint of MG on ξ^s_{cg} using the characteristic U-shaped curve of $r_{\pi,c}$, which increases by ~ 1–$2\,h^{-1}\mathrm{Mpc}$ at $r_p < 6\,h^{-1}\mathrm{Mpc}$ from the GR prediction. We find little difference between the GIK profiles predicted by the two screening mechanisms, except for slightly different trends of the radial velocity dispersion with distance.

It is unclear whether the similar signature of these two distinct modified gravity theories on GIK is a coincidence, or a generic result for any typical scalar–tensor theory that recovers the observed ΛCDM–like expansion history and reduces to normal gravity in the solar system and binary pulsars. In either case, our findings imply that, in combination with WL, galaxy infall kinematics offer a powerful non–parametric cosmological test of modified gravity. Ongoing galaxy redshift surveys will provide large samples of clusters with good statistics for measuring ξ^s_{cg} and inferring GIK out to large scales. The main systematic uncertainty arises from the imperfect understanding of the impact of galaxy formation physics on GIK. Within the context of GIK modelling and calibration, the infall behavior of realistic galaxies could differ from that of tracers in cosmological simulations (e.g., halos/sub–halos in N-body simulations, post–processed galaxies in semi–analytical galaxy formation models, and simulated galaxies in hydrodynamic simulations, etc; See Wu et al. 2013). However, we expect minimal impact on the characteristic infall velocity, which is our main tool of estimating the dynamical mass profiles of clusters, as any physical process that modifies galaxy kinematics within halos likely only adds scatter to the velocity dispersions rather than changing the mean.

Within the context of testing gravity, the effects of galaxy formation physics could be partly degenerate with those of modified gravity. The observed properties of galaxies, including luminosity, morphology, colour, star formation, and clustering, are known to correlate with the environment (see, e.g., Guo et al. 2013; Zehavi et al. 2011; Zu et al. 2008; Park et al. 2007; Kauffmann et al. 2004; Balogh et al. 2004; Hogg et al. 2003; Goto et al. 2003), and MG theories also rely on the environment to mediate the strength of the fifth force. For example, a sample of preferentially blue, star–forming galaxies may show enhanced infall velocities compared to a galaxy sample that is unbiased in colour in ΛCDM universes, and the enhancement could be mistaken as signal of modified gravity were the selection bias not properly accounted for. We will investigate the potential systematic uncertainties induced by galaxy formation physics in a future paper,
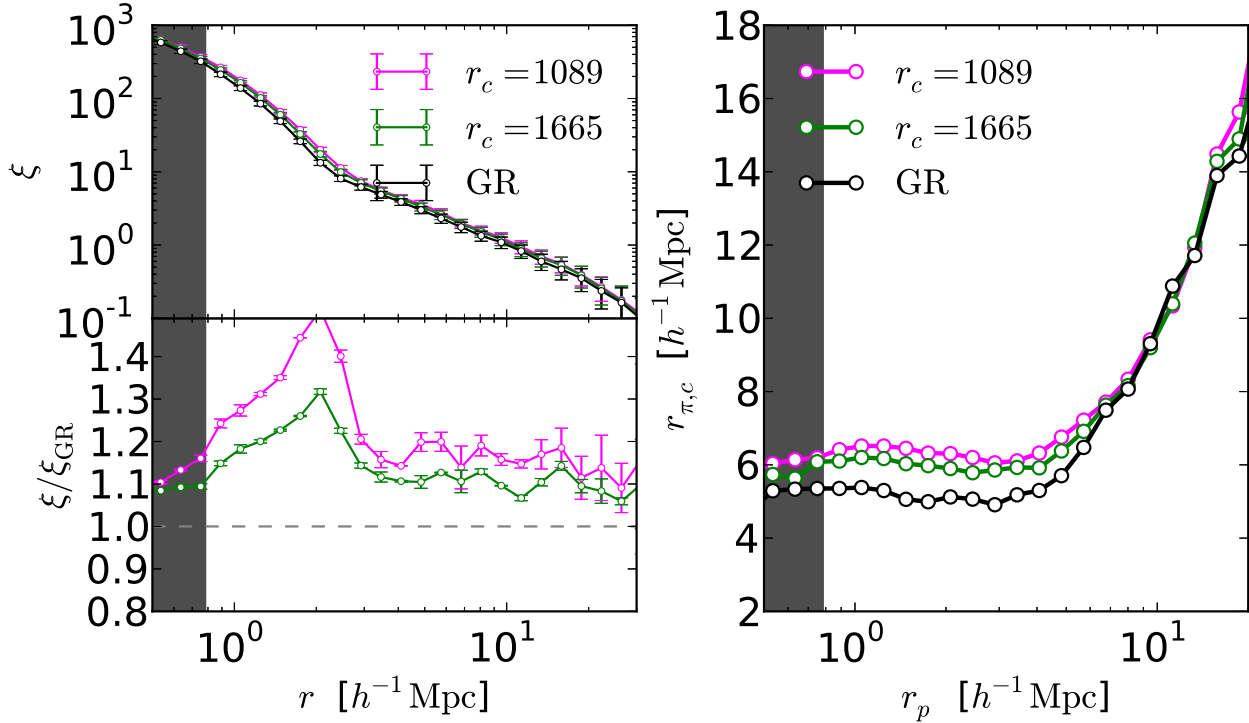
Figure 10. Similar to Figure 7, but for the Galileon simulations. The shaded region indicates the distance scale below the force resolution in the simulations.

using mock galaxy samples constructed from different HOD and semi-analytical model prescriptions. Redshift surveys that probe a range of galaxy types are especially valuable for those cosmological tests because one can check that different classes of galaxies lead to the same cosmological conclusions even though the galaxy samples themselves have different clustering and kinematics.

Our GIK modelling of ξ_{cg}^s is complementary to other semi–analytical approaches based on the halo model (Lam et al. 2013, 2012), both seeking to model the velocity distribution around massive clusters for testing gravity (also see Tinker et al. 2006; Tinker 2007, for an alternative method of modelling galaxy redshift–space distortion based on HOD). The semi–analytical velocity model adopted in Lam et al. (2013) has three components: the empirical infall velocity from the spherical collapse model, the halo-halo pairwise velocity distribution, and the intra-halo velocities (assumed Maxwellian with constant scatter). While the model itself is highly informative, the accuracy is slightly lacking compared to simulation predictions. We instead use the simulations as emulators for GIK, trading more computer time for better accuracy in the prediction of our model. In terms of observational applications, our method differs from Lam et al. (2013) in two significant aspects. First, they use the stacked redshift differences as the observable, but the model predicts the LOS velocity dispersion, so they are affected by the systematics in the subtraction of Hubble flow in the 2-halo term; in our method Hubble flow is naturally incorporated in the calculation of ξ_{cg}^s. Second, they consider the velocity distributions up to the second moment, while we are able to model the entire $P(v_r, v_t)$ including all higher moments.

Established as one of the most powerful probes of dark energy, stacked WL analysis of clusters requires deep imaging surveys that can simultaneously yield lensed background galaxies and foreground cluster sample. Forecasts for Stage III and Stage IV

dark energy experiments predict cluster WL constraints that are competitive with supernovae, baryon acoustic oscillations, and cosmic shear (see Weinberg et al. 2013, sections 6 and 8.4). To complement WL as a cosmological test of gravity, GIK modelling of galaxy clusters requires overlap with a large galaxy redshift survey, such as the ongoing Baryon Oscillation Spectroscopic Survey (BOSS, Dawson, Schlegel, et al. 2013), its higher redshift successor eBOSS (see Comparat et al. 2013), and the deeper surveys planned for future facilities such as BigBOSS (Schlegel et al. 2009), DESpec (Abdalla et al. 2012), the Subaru Prime Focus Spectrograph (Ellis et al. 2012), *Euclid* (Laureijs et al. 2011), and *WFIRST* (Green et al. 2012; Spergel et al. 2013). We expect that, in combination with the stacked cluster WL analysis, the redshift–space cluster–galaxy cross–correlations can reveal an accurate and complete picture of the average galaxy infall around clusters, allowing stringent tests of modified gravity theories for the origin of the accelerating expansion of the Universe.

REFERENCES

Abdalla F. et al., 2012, arXiv:1209.2451

Amendola L., Gannouji R., Polarski D., Tsujikawa S., 2007, Physical Review, D, 75, 83504

Amendola L., Tsujikawa S., 2008, Physics Letters B, 660, 125

Appleby S., Linder E. V., 2012, Journal of Cosmology and Astro-Particle Physics, 08, 026

Babichev E., Deffayet C., 2013, ArXiv e-prints, 1304, 7240

Baeßler S., Heckel B. R., Adelberger E. G., Gundlach J. H., Schmidt U., Swanson H. E., 1999, Physical Review Letters, 83, 3585

Balogh M. et al., 2004, Monthly Notices of the Royal Astronomical Society, 348, 1355

Barreira A., Li B., Baugh C. M., Pascoli S., 2012, Physical Review D, 86, 124016

Barreira A., Li B., Hellwing W. A., Baugh C. M., Pascoli S., 2013, Nonlinear structure formation in the cubic galileon gravity model. arXiv e-print 1306.3219

Belikov A. V., Hu W., 2013, Physical Review D, 87, 84042

Berlind A. A., Weinberg D. H., 2002, The Astrophysical Journal, 575, 587

Bertotti B., Iess L., Tortora P., 2003, Nature, 425, 374

Brax P., van de Bruck C., Davis A.-C., Li B., Shaw D. J., 2011, Physical Review D, 83, 104026

Bryan G. L., Norman M. L., 1998, The Astrophysical Journal, 495, 80–99

Buchdahl H. A., 1970, Monthly Notices of the Royal Astronomical Society, 150, 1

Budzynski J. M., Koposov S. E., McCarthy I. G., McGee S. L., Belokurov V., 2012, Monthly Notices of the Royal Astronomical Society, 423, 104

Capozziello S., Carloni S., Troisi A., 2003, Quintessence without scalar fields. arXiv e-print astro-ph/0303041, Recent-Res.Dev.Astron.Astrophys.1:625,2003

Carroll S. M., Duvvuri V., Trodden M., Turner M. S., 2004, Physical Review D, 70, 43528

Chan K. C., Scoccimarro R., 2009, Physical Review D, 80, 104005

Comparat J. et al., 2013, Monthly Notices of the Royal Astronomical Society, 428, 1498

Dawson K. S. et al., 2013, The Astronomical Journal, 145, 10

de Rham C., Gabadadze G., Heisenberg L., Pirtskhalava D., 2011a, Physical Review D, 83, 103516

de Rham C., Gabadadze G., Tolley A. J., 2011b, Physical Review Letters, 106, 231101

Dvali G., Gabadadze G., Porrati M., 2000, Physics Letters B, 485, 208

Eisenstein D. J. et al., 2001, The Astronomical Journal, 122, 2267

Ellis R. et al., 2012, arXiv:1206.0737

Goto T., Yamauchi C., Fujita Y., Okamura S., Sekiguchi M., Smail I., Bernardi M., Gomez P. L., 2003, Monthly Notices of the Royal Astronomical Society, 346, 601

Gratia P., Hu W., Wyman M., 2012, Physical Review D, 86, 61504

Green J. et al., 2012, arXiv:1208.4012

Guo H. et al., 2013, The Astrophysical Journal, 767, 122

Hayashi E., White S. D. M., 2008, Monthly Notices of the Royal Astronomical Society, 388, 2–14

Hinterbichler K., 2012, Reviews of Modern Physics, 84, 671

Hinterbichler K., Khoury J., 2010, Physical Review Letters, 104, 231301

Hogg D. W. et al., 2003, The Astrophysical Journal Letters, 585, L5

Hu W., 2009, Nuclear Physics B Proceedings Supplements, 194, 230

Hu W., Sawicki I., 2007, Physical Review D, 76, 64004

Hui L., Nicolis A., Stubbs C. W., 2009, Physical Review D, 80, 104002

Jackson J. C., 1972, Monthly Notices of the Royal Astronomical Society, 156, 1P

Jain B., Khoury J., 2010, Annals of Physics, 325, 1479

Jain B., VanderPlas J., 2011, Journal of Cosmology and Astro-Particle Physics, 10, 032

Jain B., Vikram V., Sakstein J., 2012, arXiv:1204.6044

Jennings E., Baugh C. M., Li B., Zhao G.-B., Koyama K., 2012, Monthly Notices of the Royal Astronomical Society, 425, 2128

Jing Y. P., Mo H. J., Boerner G., 1998, The Astrophysical Journal, 494, 1

Kaiser N., 1987, Monthly Notices of the Royal Astronomical Society, 227, 1

Kauffmann G., White S. D. M., Heckman T. M., Ménard B., Brinchmann J., Charlot S., Tremonti C., Brinkmann J., 2004, Monthly Notices of the Royal Astronomical Society, 353, 713

Khoury J., Weltman A., 2004, Physical Review D, 69, 44026

Khoury J., Wyman M., 2009, Physical Review D, 80, 64023

Knollmann S. R., Knebe A., 2009, The Astrophysical Journal Supplement Series, 182, 608

Lam T. Y., Nishimichi T., Schmidt F., Takada M., 2012, arXiv:1202.4501

Lam T. Y., Schmidt F., Nishimichi T., Takada M., 2013, arXiv:1305.5548

Laureijs R. et al., 2011, arXiv:1110.3193

Li B., Hellwing W. A., Koyama K., Zhao G.-B., Jennings E., Baugh C. M., 2013a, Monthly Notices of the Royal Astronomical Society, 428, 743

Li B., Zhao G.-B., Koyama K., 2012a, Monthly Notices of the Royal Astronomical Society, 421, 3481

Li B., Zhao G.-B., Koyama K., 2013b, Journal of Cosmology and Astro-Particle Physics, 05, 023

Li B., Zhao G.-B., Teyssier R., Koyama K., 2012b, Journal of Cosmology and Astro-Particle Physics, 01, 051

Lombriser L., Li B., Koyama K., Zhao G.-B., 2013, Physical Review D, 87, 123511

Lombriser L., Schmidt F., Baldauf T., Mandelbaum R., Seljak U., Smith R. E., 2012, Physical Review D, 85, 102001

Luty M. A., Porrati M., Rattazzi R., 2003, Journal of High Energy Physics, 09, 029

Mandelbaum R., Seljak U., Baldauf T., Smith R. E., 2009, 27

Mandelbaum R., Seljak U., Cool R. J., Blanton M., Hirata C. M., Brinkmann J., 2006, Monthly Notices of the Royal Astronomical Society, 372, 758

Navarro J. F., Frenk C. S., White S. D. M., 1997, The Astrophysical Journal, 490, 493

Nicolis A., Rattazzi R., Trincherini E., 2009, Physical Review D, 79, 64036

Nojiri S., Odintsov S. D., 2003, Physical Review D, 68, 123512

Olive K. A., Pospelov M., 2008, Physical Review D, 77, 43524

Park C., Choi Y.-Y., Vogeley M. S., Gott J. R., Blanton M. R., SDSS Collaboration, 2007, The Astrophysical Journal, 658, 898

Peacock J. A., Smith R. E., 2000, Monthly Notices of the Royal Astronomical Society, 318, 1144

Pietroni M., 2005, Physical Review D, 72, 43535

Reyes R., Mandelbaum R., Seljak U., Baldauf T., Gunn J. E., Lombriser L., Smith R. E., 2010, Nature, 464, 256

Schlegel D. J. et al., 2009, arXiv:0904.0468

Schmidt F., 2009, Physical Review D, 80, 123003

Schmidt F., Lima M., Oyaizu H., Hu W., 2009a, Physical Review D, 79, 83518

Schmidt F., Vikhlinin A., Hu W., 2009b, Physical Review D, 80, 83505

Scoccimarro R., Sheth R. K., Hui L., Jain B., 2001, The Astrophysical Journal, 546, 20

Seljak U., 2000, Monthly Notices of the Royal Astronomical Society, 318, 203

Sheldon E. et al., 2009, The Astrophysical Journal, 703, 2217

Spergel D. et al., 2013, ArXiv e-prints, 1305, 5422

Springel V., 2005, Monthly Notices of the Royal Astronomical Society, 364, 1105

Tinker J. L., 2007, Monthly Notices of the Royal Astronomical Society, 374, 477

Tinker J. L., Weinberg D. H., Zheng Z., 2006, Monthly Notices of the Royal Astronomical Society, 368, 85

Vainshtein A. I., 1972, Physics Letters B, 39, 393

Wang J., Hui L., Khoury J., 2012, Physical Review Letters, 109, 241301

Weinberg D. H., Mortonson M. J., Eisenstein D. J., Hirata C., Riess A. G., Rozo E., 2013, Physics Reports

Wu H.-Y., Hahn O., Evrard A. E., Wechsler R. H., Dolag K., 2013, Virial scaling of galaxies in clusters: Bright to faint is cool to hot. arXiv e-print 1307.0011

Wyman M., 2011, Physical Review Letters, 106, 201102

Wyman M., Jennings E., Lima M., 2013, ArXiv e-prints, 1303, 6630

Wyman M., Khoury J., 2010, Physical Review D, 82, 44032

York D. G. et al., 2000, The Astronomical Journal, 120, 1579

Zehavi I. et al., 2011, The Astrophysical Journal, 736, 59

Zhang P., Liguori M., Bean R., Dodelson S., 2007, Physical Review Letters, 99, 141302

Zhao G.-B., Li B., Koyama K., 2011a, Physical Review D, 83, 44007

Zhao G.-B., Li B., Koyama K., 2011b, Physical Review Letters, 107, 71303

Zheng Z. et al., 2005, The Astrophysical Journal, 633, 791

Zheng Z., Zehavi I., Eisenstein D. J., Weinberg D. H., Jing Y. P., 2009, The Astrophysical Journal, 707, 554

Zu Y., Weinberg D. H., 2013, Monthly Notices of the Royal Astronomical Society, 431, 3319

Zu Y., Weinberg D. H., Rozo E., Sheldon E. S., Tinker J. L., Becker M. R., 2012, Cosmological constraints from the large scale weak lensing of SDSS MaxBCG clusters. arXiv e-print 1207.3794

Zu Y., Zheng Z., Zhu G., Jing Y. P., 2008, The Astrophysical Journal, 686, 41